Journal of Neuroscience Methods 221 (2014) 112–126

Contents lists available at ScienceDirect

Journal of Neuroscience Methods

journal homepage: www.elsevier.com/locate/jneumeth

Basic Neuroscience

Automatic mapping of visual cortex receptive fields: A fast and precise algorithm

Mario Fiorani, João C.B. Azzi, Juliana G.M. Soares, Ricardo Gattass*

Institute of Biophysics Carlos Chagas Filho, Federal University of Rio de Janeiro, CCS, Bloco G, Ilha do Fundão, Rio de Janeiro, RJ 21949-902, Brazil

HIGHLIGHTS

- Fast and precise automatic algorithm that allows receptive field mapping.
- The method allows bias free automatic mapping of visual receptive fields.
- Algorithm reveals receptive field location and boundaries.
- Comprehensive: automatic mapping of a wide ($30^\circ \times 30^\circ$) visual field area.
- Scalable receptive field mapping that works with multi-electrodes.

ARTICLE INFO

Article history:
Received 24 July 2012
Received in revised form
12 September 2013
Accepted 20 September 2013

Keywords:
Bias-free receptive field mapping
Visual system
Topographical visual areas
Monkey

ABSTRACT

An important issue for neurophysiological studies of the visual system is the definition of the region of the visual field that can modify a neuron's activity (i.e., the neuron's receptive field – RF). Usually a trade-off exists between precision and the time required to map a RF. Manual methods (qualitative) are fast but impose a variable degree of imprecision, while quantitative methods are more precise but usually require more time. We describe a rapid quantitative method for mapping visual RFs that is derived from computerized tomography and named back-projection. This method finds the intersection of responsive regions of the visual field based on spike density functions that are generated over time in response to long bars moving in different directions. An algorithm corrects the response profiles for latencies and allows for the conversion of the time domain into a 2D-space domain. The final product is an RF map that shows the distribution of the neuronal activity in visual–spatial coordinates. In addition to mapping the RF, this method also provides functional properties, such as latency, orientation and direction preference indexes. This method exhibits the following beneficial properties: (a) speed; (b) ease of implementation; (c) precise RF localization; (d) sensitivity (this method can map RFs based on few responses); (e) reliability (this method provides consistent information about RF shapes and sizes, which will allow for comparative studies); (f) comprehensiveness (this method can scan for RFs over an extensive area of the visual field); (g) informativeness (it provides functional quantitative data about the RF); and (h) usefulness (this method can map RFs in regions without direct retinal inputs, such as the cortical representations of the optic disc and of retinal lesions, which should allow for studies of functional connectivity, reorganization and neural plasticity). Furthermore, our method allows for precise mapping of RFs in a 30° by 30° area of the visual field for an array of microelectrodes of any size in less than 6 min.

1. Introduction

Topographic representation is an important feature of the organization of the nervous system, especially in the early stages of sensory processing. In the visual system, the caudal areas contain neurons with relatively small receptive fields (RFs), and most cortical visual areas show some degree of topographic organization. Barlow et al. (1967) coined the term "minimum response field" to define a region in visual space in which stimuli can reliably drive a neuronal response. This term contrasts the wider concept of the RF, which includes other regions surrounding the minimum response field that can only modulate the neuronal response.

The mapping of visual cortical RFs was described by Talbot and Marshall (1941), who projected visual stimuli on a screen while recording electrophysiological responses in the cortex of an anaesthetized animal. Presently little improvement has been made

* Corresponding author. Tel.: +55 21 25626561; fax: +55 21 2808193.
E-mail addresses: rgattass@gmail.com, rgattass@biof.ufrj.br (R. Gattass).

0165-0270
http://dx.doi.org/10.1016/j.jneumeth.2013.09.012

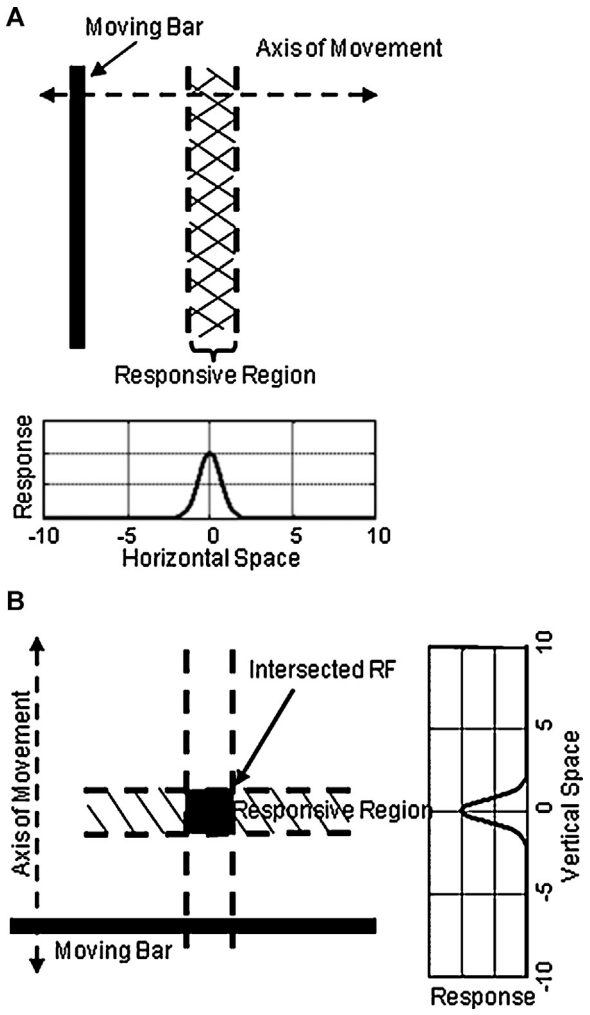

Fig. 1. Schematic of manual RF mapping with the qualitative interpolation method. When a long bar is swept across the visual field, the neuronal responses change as the stimulus passes over the neuron's RF. This example shows an excitatory neuron whose theoretical RF response profiles are shown in the graphs oriented according the axis of stimulus motion. (A) While moving a vertical bar back and forth along the horizontal axis, the experimenter marks the beginning and the end of the change in activity. As the experimenter does not know the position of the RF along the stimulus length, the entire possible region is delimited with two lines parallel to and the same length as the stimulus (vertical dashed lines). (B) The same procedure is conducted with a stimulus that is orthogonal to the first stimulus to delimit a horizontal responsive region. The intersection of the two responsive regions is then assumed to be the location of the RF (the black square).

over the manual (qualitative) mapping procedures employed by these authors. Qualitative RF mapping methods typically rely on an experimenter's ability to discriminate changes in neuronal activity usually through auditory monitoring. Two quick qualitative mapping procedures are widely used. The more intuitive one uses the intersection of the regions that responsive to orthogonal moving stimuli (Fig. 1) to determine a square portion of the visual field that elicits neuronal responses. This procedure is based on perceivable responses to both stimulus orientations. However, in some cortical areas, such as V1, most cells are orientation selective and may produce very poor or no responses to stimuli that are oriented orthogonally to the preferred orientation.

A second qualitative mapping procedure, which uses only small and well-orientated stimuli, avoids the orientation selectivity issue and is, therefore, used more generally (Hubel and Wiesel, 1962; Barlow et al., 1967; Dow et al., 1981; Gilbert et al., 1996). First, the best stimulus orientation (the one that produces the highest neuronal firing rate) is defined, and the limits of the neural response to this orientation are drawn along the axis of the movement of the stimulus (like Fig. 1A). The stimulus at the best orientation is then moved back and forth along the stimulus length to one side until no response is observed. Then, the border of the RF is drawn for that side, and the procedure is repeated for the other side of the receptive field.

Quantitative methods have been used to validate the use of a quick qualitative method (Dow et al., 1981), but the measurements of qualitative RFs have produced contradictory results. Studies using quantitative methods have shown that even the procedure used by Nobel Prize awardees Hubel and Wiesel (1962, 1968, 1974) exhibits a certain degree of inaccuracy due to the subjectivity of the manual plotting method used to map RFs (Dow et al., 1981; Das and Gilbert, 1995). Qualitative methods rely on our ability to perceive changes in neuronal responses and usually only the hot spot of the RF is mapped. In addition, these methods depend on a high signal to noise ratio, so precision decreases drastically for low-response neurons. Another source of imprecision in qualitative RF mapping is related to the parallax that arises during manual plotting by the experimenter.

Quantitative methods are more precise but usually require more time to map the RFs; therefore, most quantitative methods exhibit a trade-off between spatial resolution and the time required to map the RF. The most popular quantitative methods are based on two-dimensional arrays of either small flashing or moving stimuli or linear arrays of small moving bars, and the RFs are recovered using the reverse correlation technique (Palmer et al., 1987). In all cases, the stimulus size and separation define the methodological resolution. For example, mapping a 30° by 30° region of the visual field with 1° resolution (i.e., very poor resolution) requires the testing of 900. Using the lowest stimulus density, one position per frame, at 60 Hz, it takes 15 s to test these 900 positions. To obtain the 20 trials per position needed for statistical reliability, 5 min are required. If a 0.5° resolution is used (which is still a rather poor resolution), 3600 positions have to be tested at a cost of 20 min. Thus, every doubling of the map resolution increases the mapping time by a factor of four. Usually, these procedures are employed only in special circumstances in which quantitative spatial precision is crucial or to unveil the fine spatiotemporal relationships of the response (see Colby et al., 1996; Duhamel et al., 1997, 1998).

As time and accuracy are major issues in electrophysiological experiments, we have implemented a back-projection method for the mapping of visual RFs, and tested this method exhaustively over the last 10 years. This method can determine, in a few minutes, the precise locations and sizes of RFs from an extensive area of the visual field. The algorithm can be implemented for many recording sites, and the time needed for mapping is independent of the number of electrodes used.

2. Materials and methods

2.1. The back-projection mapping method

The quantitative mapping method evaluated here is a combination of the qualitative intersection method described in Fig. 1 and an old and simple digital signal processing technique called back-projection that is widely used in computerized tomography. This method builds up a two-dimensional image from 'one-dimensional (linear) views' taken from distinct points of view in the same plane (see Smith, 1999; Herman, 2009).

Although we know that neuronal latency is an important issue for this method, for simplicity, we will assume that the profile of the recorded neuronal response to a moving stimulus passing through an RF is spatially aligned with the receptive field, and the abscissa represents the axis of movement space (Fig. 2A and B). Similar to

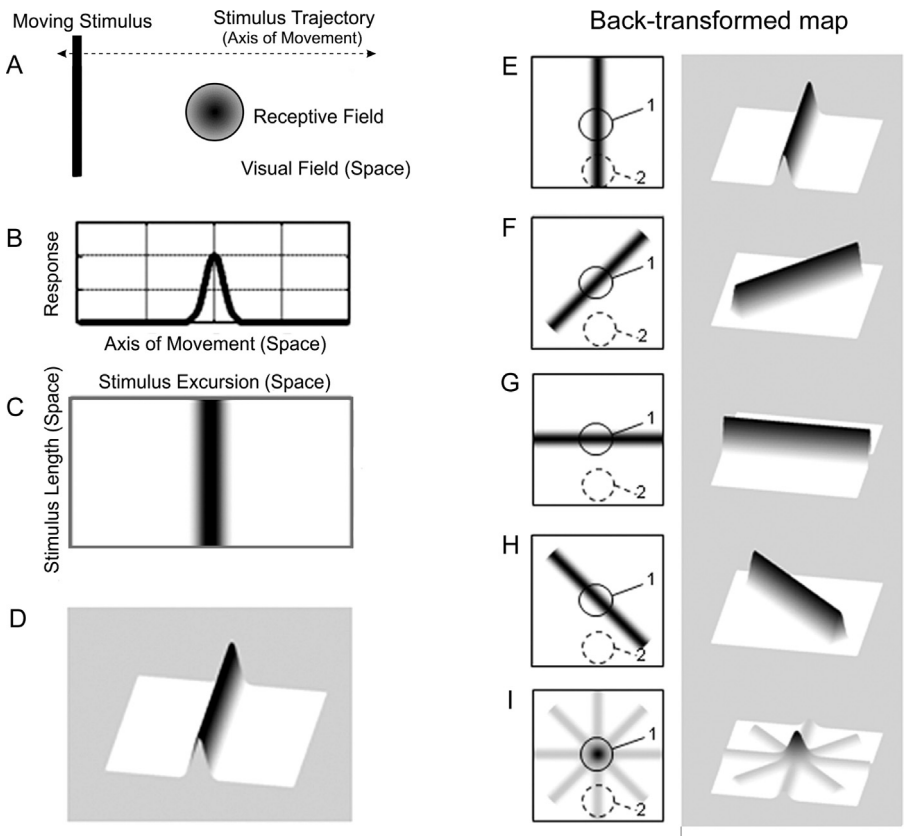

Fig. 2. Representation of an RF response along an axis of movement (left) and the back-projection map (right): (A) The stimulus, a moving bar, passing through the RF. (B) The RF response profile along the length of motion. (C) Representation of the replicated RF response profile along the length of the stimulus, gray-scale coded. (D) A 3D view of the representation in C. The responses to the bar moving in each axis (E–H) are averaged to generate the back-projection map (I). Circle 1 marks the location of the RF; i.e., the site at which all responsive regions intersect and are averaged together. Circle 2 marks a responsive region outside the receptive field that does not intersect other responsive regions and is averaged out by the other non-responsive regions.

qualitative mapping (Fig. 1), as we do not know where the RF is located along the stimulus length, we replicate the response to represent all possible points under the stimulus length (Fig. 2C and D). The result is a map of the neuronal activity in the visual space domain scanned by moving the stimulus along a specific axis of movement. The size of this map, in terms of the visual field, is the product of the stimulus excursion and the stimulus length, and the intensity of the neuronal activity is represented along the third axis (or on a pseudo color scale). When there is a clear response to a given stimulus, the axis of movement (or the direction) map will show the region corresponding to the RF as a ridge of increased activity.

When maps from different axes of movement (Fig. 2E–H) are averaged (Fig. 2I), the responsive regions that intersect each other maintain their mean value (Fig. 2E–I, region 1), while the regions that do not intersect will be diluted by the non-responsive regions (Fig. 2E–I, region 2). The final result is a back-projection map with a single peak at the intersected region, which corresponds to the actual RF (Fig. 2I). Therefore, back-projection is a method for revealing the intersection of the responsive regions in the visual field for stimuli moving in different directions that is the quantitative equivalent of the qualitative method described in Fig. 1. Although they are diluted by averaging with many non-responsive regions, some non-intersecting response artifacts remain in the final back-projection map. We call the asterisk-shaped ridges around the RF ridge artifacts. The amplitude of the ridge artifacts is directly proportional to the response amplitude in the orthogonal orientation and inversely proportional to the number of axes of movement used. Larger numbers of axes result in greater dilution of the ridge artifacts caused by activity outside the intersection region (map peak).

Back-projection maps can be obtained using the algorithm described in the Appendix (implement in MATLAB, MathWorks Inc.). This script allows the use of any number of direction projections (neuronal responses). In addition to the intersected response back-projection map, a variance map can also be generated.

2.1.1. *The latency problem*

There is a finite amount of time between retinal stimulation and neuronal responses and, as mentioned earlier, this neuronal latency is an important issue for the spatial precision of back-projection maps. This latency produces neuronal responses (Fig. 3A) to moving stimuli that are delayed relative to the position of the stimuli along its trajectory (Fig. 3B1 and B2). If we consider two opposite directions, each peak of the responses over time will be displaced to alternate sides (Fig. 3B1) relative to the actual spatial position of the RF (Fig. 3A). Because opposite directions are averaged together in the back-projection mapping procedure, maps without latency corrections exhibit some imprecisions (Fig. 3C1). If the response amplitudes for the opposite directions are equal, the center of the RF (map peak) will be estimated in the correct position, but the extent of the RF will be overestimated (Fig. 3C1). The worst-case scenario occurs when the responses exhibit a directional preference, which results in different amplitudes for the opposite directions. In this case, both the peak position and the extent of the RF will be imprecise (Fig. 3D1). The peak will be displaced towards the preferred direction (larger response), and the size will be overestimated. As the back-projection map averages the responses for all directions

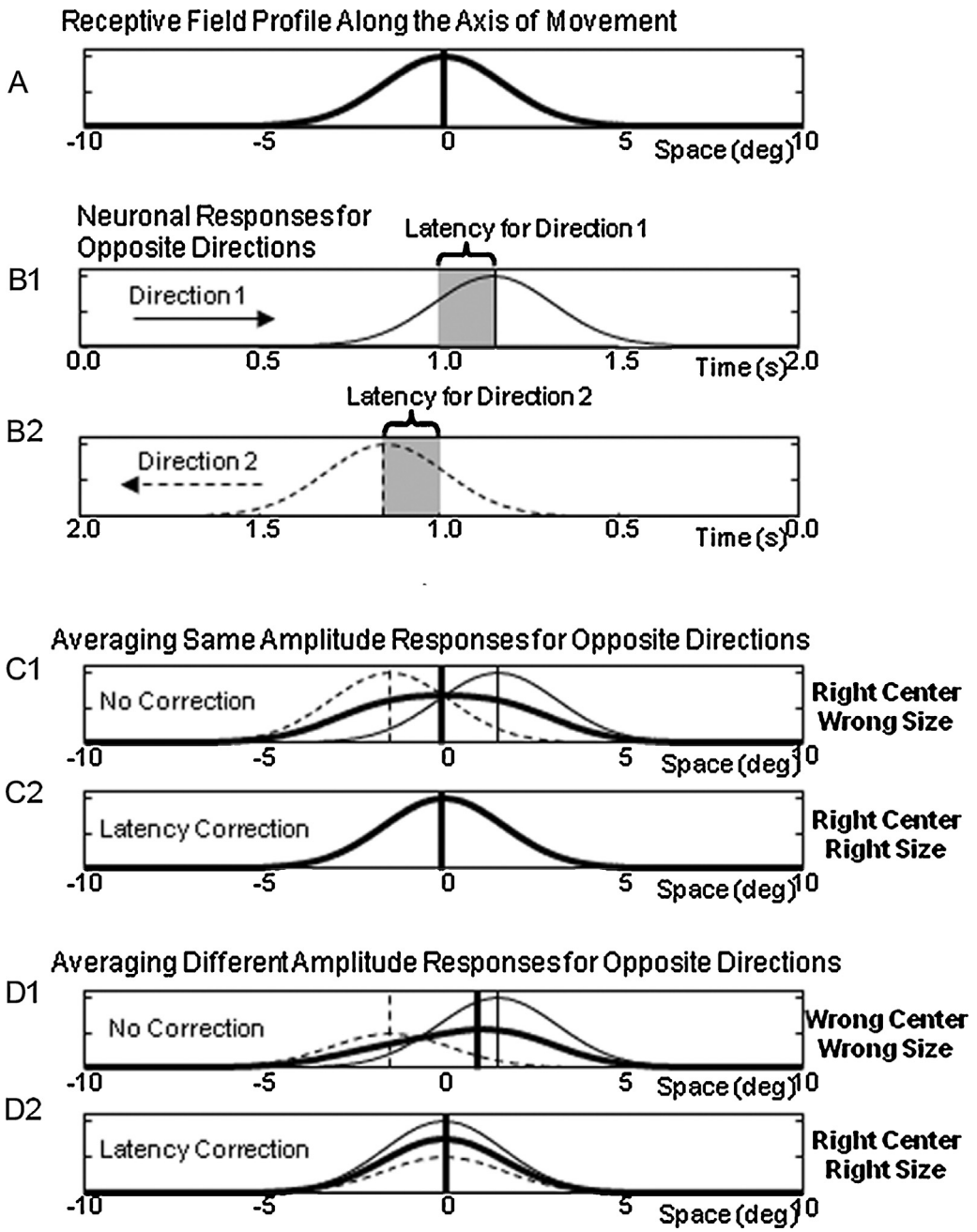

Fig. 3. Relationship between a stimulus, the receptive field, and the response field profile along the axis of movement. (A) RF profile along the axis of stimulus movement. (B) The neuronal latency displaces the response position in the same direction the stimulus is moving (B1 and B2). The conversion from time to spatial coordinates combines (averages) stimuli moving in opposite directions. (C) Averaging neuronal responses of the same amplitude for opposite directions without latency correction (C1) produces an average response that is in the correct position but overestimated in size. The same averaging after a latency correction (C2) results in the correct response profile in terms of both position and size. (D) Averaging neuronal responses of different amplitudes for opposite directions without latency correction (D1) produces an average response that is in the wrong position with an overestimated size. The same averaging after latency correction (D2) results in the correct response profile in terms of both position and size.

together, the absence of a latency correction will diminish the precision of the mapped RF, and thus latency should be corrected for before constructing the back-projection map. With the correction, the peak response and extent are precise (Fig. 3C2 and D2). The influence of the latency correction on the mapping precision will be evaluated later using data simulations.

2.2. Data simulation

Simulated response time histograms with controlled RF positions, sizes and spike probabilities were generated to quantitatively test the back-projection mapping procedure. The spike probabilities were based on normally distributed random values.

The response histograms for each stimulus direction were generated by averaging a number of trials (10 in most cases). To generate each simulated trial (raster), first, theoretical probability response curves simulating the RF were constructed (Fig. 4A and D – black lines). For each point of the curve (bin), a normally distributed random value was sampled, if the value was equal or above the probability value of the theoretical response curve, a single spike was added to the equivalent time point in the raster (Fig. 4A and D – light blue ticks). Like the theoretical response curve, the resulting

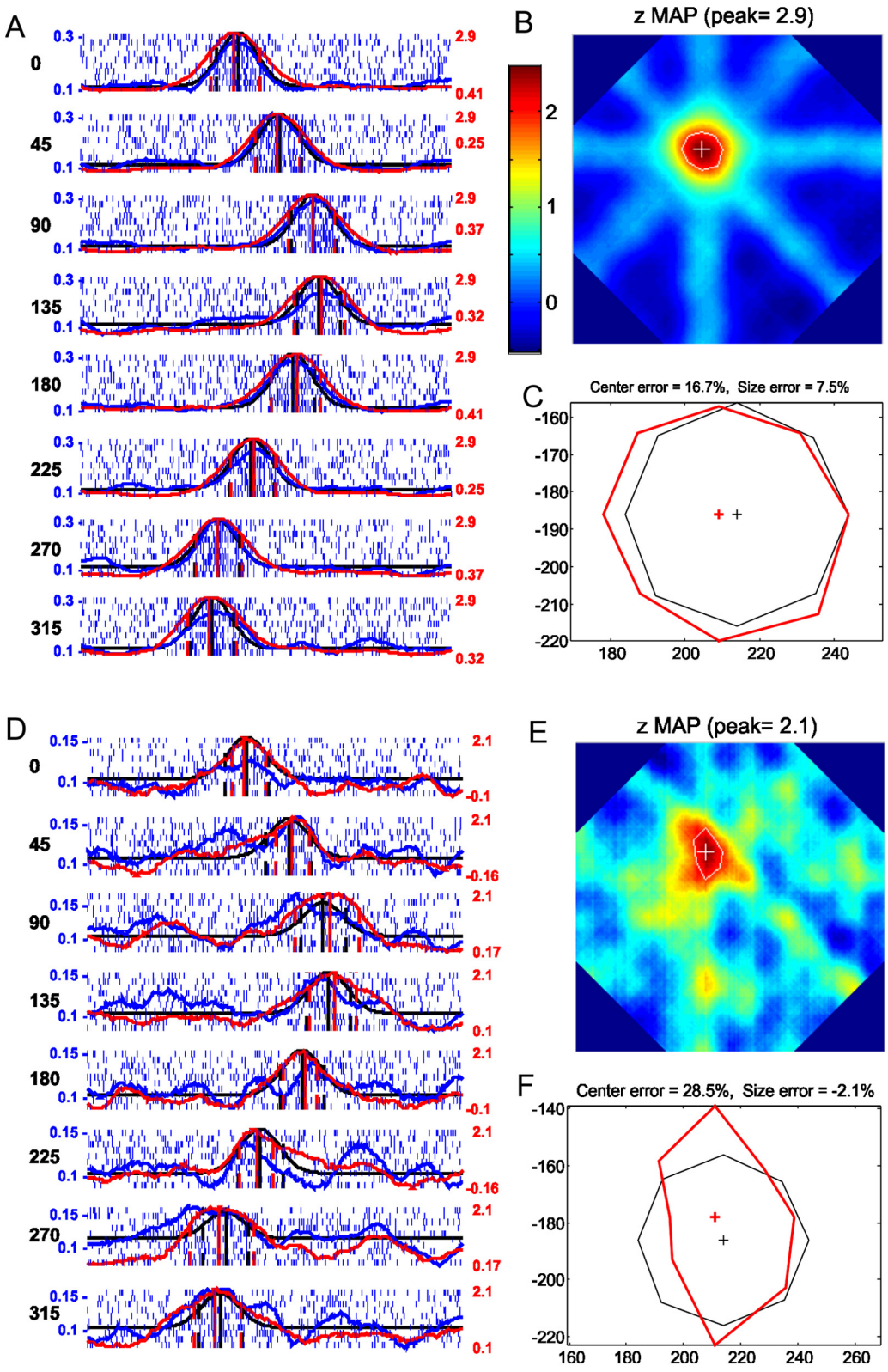

Fig. 4. Relationship between the simulated and the mapped RFs for two simulations with different response levels. (A–C) represents the mapping for a high probability response ($p = 0.3$), and (D–F) represent the mapping for a low probability response ($p = 0.05$). (A and D) responses for 8 directions. The black lines represent the spike probabilities for the theoretical RF. The light blue ticks represent the spikes for 10 simulated rasters, and the blue lines represent the smoothed response histograms. The probability values are shown on the left axis in blue. The red lines represent the response profiles obtained from the back-projection maps illustrated in B and E, and the *z*-score values are shown on the right axis in red. C and F show comparisons of the theoretical RFs (in black) and the mapped RFs (in red). (For interpretation of the references to colour in this figure legend, the reader is referred to the web version of the article.)

histograms (Fig. 4A and D – blue lines) expressed the probability of the occurrence of a spike. This procedure allows for small variations in the responses and, like real neurons, exhibits a variance that increases proportionally with the response (up to a probability of 0.5). Typically, we used 501-point response vectors corresponding to the 'stimulus excursion' with RFs sizes ranging from 5 to 20 points. The positions of the receptive fields were also varied systematically.

2.2.1. Signal/noise ratio

Fig. 4 shows the precision of the automatic mapping of two simulated units, one with a high signal/noise ratio (Fig. 4A–C) and another with a low signal/noise ratio (Fig. 4D–F), studied with 10 trials, 8 directions of movement and smoothing with a Gaussian convolution (of 150 ms = 5 pixels). In this example, we show spike rasters for each trial and each direction. Evaluation of the cell's response based on individual rasters is quite difficult but becomes simple when all trials (80) are averaged. The precision of the algorithm was evaluated by generating a theoretical RF in a matrix of 501×501 pixels. If the RF was centered in the spatial map, it had a diameter of 51 pixels at 73% of the peak high, and 60 pixels at half the peak height. For each simulation, we show a theoretical spike probability curve that illustrates the RF being simulated and a simulated response curve that should reflect the theoretical curve (Fig. 4A and D). This procedure allowed us to compare the theoretical RF with the RF obtained with the back-projection map (Fig. 4C and F). The main RF parameters we compared here were the RF center and the RF size. The error in finding the correct RF center is expressed as a percentage of the theoretical RF radius (half size), and the error in finding the correct RF size is expressed as a percentage of the RF diameter (size). In the case of the unit with the high signal/noise ratio, the simulated rasters for each trial in each direction with the corresponding standardized response histograms (*z*DFs) are shown in Fig. 4A. The automatically mapped receptive field shows remarkable precision (Fig. 4B). Fig. 4C shows that the borders of the simulated and mapped RFs had a difference (error) of 7.5%. This figure also shows that the location error was 16.7% of the RF radius. Fig. 5E shows a reasonably precise, but noisy, receptive field that was automatically mapped based on the data illustrated in Fig. 4D. Fig. 4F shows that the borders of the simulated and mapped RFs had a difference (error) of −2.5%. This figure also shows that the location error was 28.5% of the RF radius.

2.3. Electrophysiological data

The automatic quantitative method was evaluated with data from other electrophysiological studies that used anesthetized adult *Cebus apella* monkeys. All experimental protocols were conducted following the National Institutes of Health (NIH) guidelines for animal research and were approved by the Committee for Animal Care and Use of the Instituto de Biofísica Carlos Chagas Filho, Federal University of Rio de Janeiro. The procedures were similar to those used by Gattass and Gross (1981), Fiorani et al. (1989), and Botelho et al. (2012).

2.3.1. Visual stimulation and data acquisition

Gas-permeable contact lenses were used to focus the eyes on a computer monitor placed 57 cm in front of the animal. The positions of the blind spot and fovea were plotted onto the computer screen using a reversible ophthalmoscope. Synchronization of stimulus generation and data acquisition was performed with the CORTEX program (NIH, Bethesda, MD, USA). The stimulus consisted of a thin white bar ($0.2^\circ \times 30^\circ$) that appeared over a dark background in one of four random orientations (0°, 45°, 90°, or 135°) and crossed the screen in one of the directions perpendicular to its orientation at a velocity of 10°/s (3 s/trial). This stimulation allowed for the scanning of an area of approximately $30^\circ \times 30^\circ$. Each direction was tested 10 times (10 trials) to produce a final data set of 80 trials. With this protocol, we were able to study an area of $30^\circ \times 30^\circ$ of the visual space in 4 min (80 trials × 3 s).

Extracellular multi- and single-unit activities from cortical visual areas were recorded using tungsten microelectrodes. The activity was amplified and filtered between 0.7 and 6 kHz (HST/16o25 headset, 32-channel pre-amplifier box, Plexon, Dallas, TX, USA) before being digitized at 32 kHz by a high-speed, 16-bit resolution A/D card (PCI-6259, National Instruments, Austin, TX, USA). Data acquisition and storage were controlled by custom-written software (SPASS, Max-Planck Institute, Frankfurt).

2.4. Data preprocessing

2.4.1. Spontaneous activity

To accurately find the receptive field size, the background or spontaneous activity has to be determined. Although spontaneous activity can be recorded separately, it can be easily obtained from the direction histograms using the back-projection map itself. In a coarse first approximation of the RF map, a reasonable amount of imprecision is obtained when averaging the response with the spontaneous activity. Once the RF position is found using the back-projection map, all activity outside the RF can be considered as spontaneous activity.

2.4.2. Response standardization (z-score)

To compare neurons with different firing rates and to create a statistical estimate of the peak values in the back-projection map, we normalized the neuronal response by their *z*-scores. The *z*-score expresses the extent to which the response at each point differed from the baseline activity in terms of standard deviations (SDs). As we aimed for the baseline data to be zero, we first subtracted the overall mean spontaneous activity from the histogram and then divided that activity by the SD of the activity.

$$z = \frac{(\text{data} - \text{spontaneous})}{\text{SD}}.$$

The SD was calculated centered on zero to create an SD that represented how far the data were from baseline. This calculation was achieved by computing the square root of the mean squared data.

$$\text{SD} = \text{square root}\left(\frac{\text{sum}(\text{data}\hat{}2)}{(n-1)}\right)$$

When the spontaneous activity was not available, for example, when we computed latencies, we use the regular *z*-score centered in the mean activity.

$$z = \frac{(\text{data} - \text{mean}(\text{data}))}{\text{SD}(\text{data})}$$

The *z*-score standardization can be performed for the data for all directions together, i.e., a simple *z*-score scaling of the neuronal responses, or this standardization can be performed for each direction independently. For direction/orientation selective neurons, independently calculated *z*-scores show the 'significance' of the response in the RF for each direction, and as the SD is directly proportional to the intensity of the response, this process decreases the differences in the responses for different directions. As will be seen in Section 3, calculating *z*-scores independently for each direction slightly, but significantly, improved the precision of the inferred RF sizes and significantly improved the precision of the RF aspect ratio.

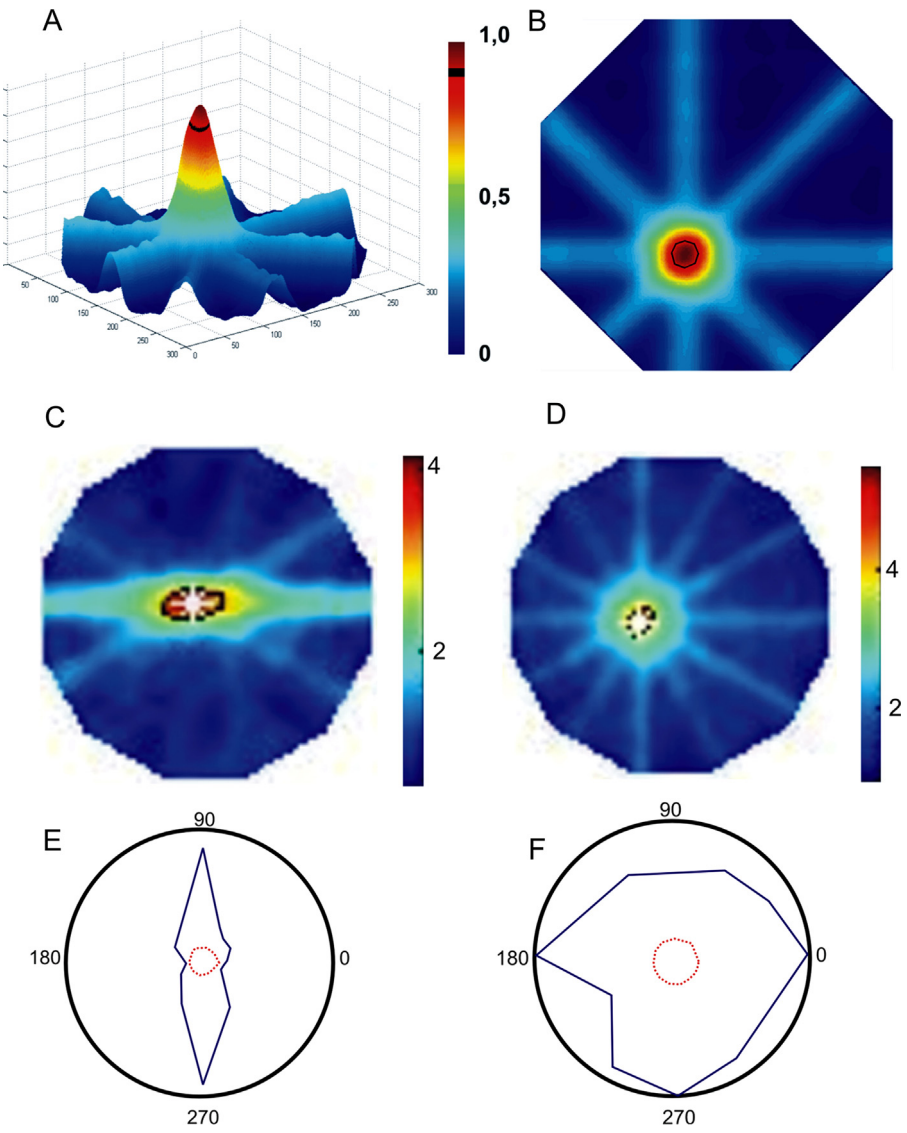

Fig. 5. Multidimensional representation of bias-free receptive-field mapping; location and moving bar receptive field size. (A) A 3D representation of the neuronal response (quantitative intersection map) elicited by a thin bar moving in 8 directions. (B) A 2D representation of the quantitative intersection map used to determine the size and location of the receptive field (dashed black circle) using a peak criterion of 90%. RF maps from a directionally selective cell (C) and from a pan-directional cell (D). Polargrams from these cells are shown in (E) and (F), respectively. Doted red circles – spontaneous activity.

2.4.3. Histogram smoothing (low pass filtering)

Even binned histograms of neuronal responses have high frequency components. These high frequency components markedly decreased the precision of RF mapping, especially at the center (peak) position. In the present method, this component was filtered out by smoothing the histogram using a normal convolution filter. We empirically determined (see Section 3) that the width of the convolution should be about the size of the expected RF. The result is a *z*-score density function (*z*DF) that expresses the instantaneous *z*-score at each bin.

2.4.4. Inhibitory responses

Some neurons exhibited responses below the spontaneous activity for some (or even all) directions of stimulation. This inhibitory activity reflects inhibitory responses (negative values) in the *z*-score. The advantages of the back-projection map in averaging out RFs from responses in different directions can be negated if inhibitory responses are present: the inhibitory responses can average out the excitatory responses and may impair the identification of the RF. The use of the absolute *z*-score (converting negative to positive values) allowed inhibitory activities to be represented as positive responses and to sum with the excitatory activities in the map. Moreover, the use of absolute *z*-scores results in fully inhibitory RFs being shown as positive peaks in the back-projection maps, which allows the same algorithm to be used to produce parameters for both excitatory and inhibitory RFs.

2.4.5. Latency correction

We have employed an empirical but very robust method for calculating latencies using the back-projection method itself. This method consists of producing many back-projection maps that systematically vary the latency corrections for the neuronal responses and then determining which latency correction results in the highest response peak. Usually, the highest peak is obtained when all the responses peaks coincide (intersect) in the map, which indicates the best common latency for all directions.

After latency correction, the histograms represent neuronal activity over space and are ready to be processed by the back-projection function. Because it takes an appreciable amount of time to produce the back-projection map when long direction vectors

are used, the latency can be tested using a restricted part of the map after finding the coarse RF position in the full map.

2.5. Back-projection map and post-processing

2.5.1. Producing the map and the RF center

The *z*DFs in spatial coordinates for all directions and the respective direction values (angles) are given to the back-projection function (see Appendix A), which generates the back-projection map that represents the average back-projected responses in the stimulated area. If there is a responsive RF inside this area, it appears as a single response peak in the map, and its position represents the RF center. The map peak value is the average RF center *z*-score and reflects the standardized strength of the mapped RF.

2.5.2. The map response profiles

The map response profiles for each stimulus direction correspond to the activities in the map passing through the peak (RF center) in the appropriate direction. Therefore, one map response profile is found for each direction of stimulation, and this profile defines the RF position in each histogram. Because of the ridge artifact, the baseline of the map response profiles may not correspond to the background activity. If orthogonal stimuli are used to produce a map because each artifact ridge is orthogonal to the direction of stimulation, the baseline activities of the map response profiles will correspond to the orthogonal ridge and represent the mean orthogonal activity divided by the number of mapping directions. All stimuli sets that contain a multiple of four numbers of directions will always have orthogonal stimuli for all directions. As most stimuli used for RF mapping deploy sets of orthogonal directions, all map response profiles will be found on top of the ridge artifact. Nevertheless, the zero value in the map response profiles will correspond to the baseline activity if the spontaneous activity has been removed.

2.5.3. RF size

In addition to being an important functional parameter, RF size is also important for defining the parts of the histograms (and also in the rasters) from which the responses should be obtained to compute the neuronal response for each direction (see Section 4). The definition of actual RF limits is hard to implement due to the slow transition between the background (spontaneous) activity and the RF-driven activity. Additionally, the back-projection maps show ridge artifacts and enlarged response profiles. The enlarged map RF is the consequence of the projection of the oblique responses, and the ridges reflect the 'averaged out' activity outside the RF for each orientation. These ridges decrease the possibility of getting the RF size at the baseline (the spontaneous activity) and force the definition of a response level (a cutoff value) in the map peak to extract the RF profile. Fortunately, Gaussian smoothing and the back-projection itself artificially enlarge the mapped RF and allow the RF to be identified at a level higher than that of the ridge artifacts.

With the parameters defined here (the number of directions and smoothing window size), we found that a cutoff value of 0.76 of the height of the map response produced RFs that corresponded to the size of the neuronal responses at half peak.

3. Results

First, we will show some examples of primate cortical RFs mapped with the back-projection method to provide support to the notion that this procedure is precise, scalable, and comprehensive. Later, we will analyze the precision of back-projection mapping using controlled simulated data.

3.1. RF mapping

The following examples show data from neurons of primate visual areas V1 and V2. The automatic mapping method can be used with any number of electrodes. An example of the processing involved in a RF mapping is illustrated in Fig. 7. The visual RFs driven by stimuli moving in eight directions were revealed by recording the neuronal responses over the entire whole length of the movement of each stimulus. The stimuli moved at 10°/s to cover a 30° excursion in 3 s. The neuronal responses to 10 trials in each direction were averaged and binned in 10 ms bins to avoid large arrays. This procedure resulted in 300 point vectors that encoded stimulus excursion with a spatial resolution of 0.1°/bin. These histograms were used as the raw neuronal responses to obtain the back-projection maps.

3.1.1. Mapping the RF: The back-projection map

If there is a relatively substantial response in the *z*DFs, a single and prominent peak will emerge in the back-projection map. The peak *z*-score will be proportional to the statistical significance of the found RF. Usually, with more than 30 samples (here we are averaging 80 trials to produce the map peaks), the statistical probabilities of *z* values being greater than 1.96 due to chance 0.05. In this example, we found a highly significant peak (z-score = 2.6; $p = 0.01$) that represented the RF center. The RF borders, which correspond to the extension of the neuronal response at half peak height, were found at 0.76 of the map peak height. This threshold height value was previously empirically determined in our population (see also the simulated data tests below). Once the position of the RF center and its borders are obtained, it is trivial to locate the responsive regions that correspond to the RF in each response histogram. In addition to providing the topography of the RF, those responses also reflect functional properties of the neuron. For example, the response levels to each direction can be expressed in a polar graph (Fig. 5E and F) and used to calculate direction and orientation selectivity indexes.

In Fig. 5, three V2 RFs are illustrated. One RF mapped with 8 directions is illustrated in 3D (Fig. 5A) and 2D (Fig. 5B), and two RFs mapped with 12 directions are illustrated in Fig. 5C and D with their respective direction polargrams (Figs. 5E and F). The color-coded 2D representation of a bi-directional receptive field is illustrated in Fig. 5C. Another 2D representation of a non-directional selective V2 cell is shown in Fig. 5D. The computations of the orientation selectivities of the cells and their spontaneous activities are illustrated in the polargrams located adjacent to the RF representations (Fig. 5E and F). Note that the neuron represented in Fig. 5C and E is strongly selective for a horizontal stimulus moving up and down, while the other neuron is not (Fig. 5D and F).

3.1.2. Electrode arrays

We used electrode arrays to record simultaneously from a large number of neurons during the same stimulation; i.e., the 4 min of stimulation of our mapping procedure that included 10 trials in each of the basic 8 directions. Fig. 6 shows examples of multiunit activity RFs created from arrays of 16 and 32 microelectrodes located in area V1.

In the first example, a 16-microelectrode array allowed the simultaneous quantitative mapping of 14 RFs (Fig. 6A). Only two electrodes (channels 3 and 4) failed to show distinctive peaks with *z*-scores greater than 1.96. When all mapped RF profiles were plotted together, the region of the visual field covered by the electrode array was revealed and showed the topographic organization of V1 (Fig. 6B).

In the 32-electrode array experiment example, 30 electrodes showed clear RFs during this recording (Fig. 6C). With the exceptions of channels 5 and 6, all recordings showed clear peaks in the

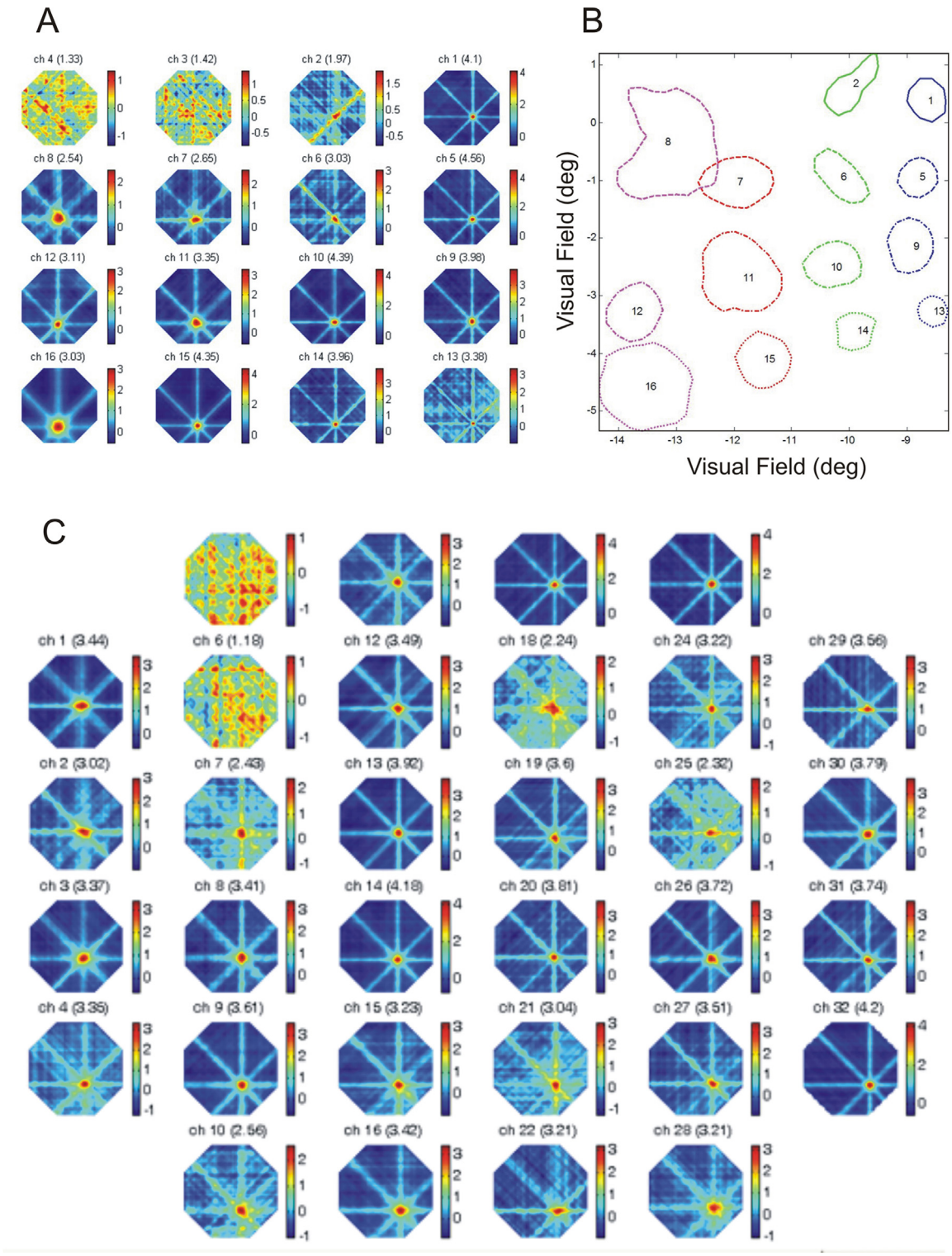

Fig. 6. Examples of simultaneous automatic mapping in V1 and the corresponding visual topographies. (A) Example of simultaneous automatic mapping with 16 electrodes. Receptive fields in V1 appear in red at the center of the ridge artifacts for 14 of the electrodes (except for channels 3 and 4). Each map (blue hexagon) represents a 30° by 30° region of the visual field, and the color scale represents the signal/noise ratios. (B) Representation of the visual field showing the receptive field borders of V1 neurons and the resulting visual topographies. (C) Example of simultaneous automatic mapping with 32 electrodes. Receptive fields appear in red at the center of the ridge artifacts for 30 of the electrodes (except for channels 6 and 7). Each map (blue hexagon) represents a 30° by 30° region of the visual field, and the color scale represents the signal/noise ratios. (For interpretation of the references to colour in this figure legend, the reader is referred to the web version of the article.)

maps and good *z*-scores. The locations of the receptive field centers varied systematically following the visual topography of V1.

3.2. Population data

3.2.1. Smoothing

After empirically testing a wide range of widths for the Gaussian convolution, we found that widths in the range of 1–2 times the size of the expected RF were optimal for revealing RF positions and sizes. Usually, there was a small tradeoff between the precision of the determination of the RF center, which was favored by smaller convolution widths, and the precision of the determination of the size, which was favored by larger widths. Nevertheless, those differences were small, and because center and size are not dissociable we did not used different convolution width values for center and size. Typically, we used convolution widths in the range of 0.6–1.2° for recordings in area V1.

3.2.2. Latency

As mentioned in Section 2, latency correction is a major issue for precise back-projection mapping. In addition to being a factor that must be corrected for, latency is an important functional property of neurons and reflects the information pathway from the photoreceptors to the recorded neuron. In one set of data in which we recorded approximately 400 V1 neurons, we estimated the neurons' latencies by testing values that varied from 0 to 120 ms in 1 ms steps. The neurons tested at approximately 15° – eccentricity in V1 showed latencies in the range of 50–80 ms. The average latency for this V1 population was 74 ms. All data illustrated herein are corrected for latency.

3.3. Controlled back-projection map tests

As real RFs exhibit individual imprecision due to the stochastic nature of neuronal responses and also exhibit intrinsic functional disparity preferences, it is difficult to test the accuracy of the back-projection method with real data. To solve this problem, we used controlled, artificially generated data that simulated neuronal responses to moving bars; these data were generated based on theoretical RFs, and we compared the observed back-projection RF maps with the theoretical RF maps (see Section 2).

3.3.1. Smoothing Gaussian width

We tested our Gaussian smoothing using the size of the RF as a reference. Fig. 7 shows the comparison of the precision of the automatic mapping of a 1.5° × 1.5° (5 × 5 pixels) RF from a simulated unit with a low signal/noise ratio (0.15) studied with 10 trials and 8 directions with and without a Gaussian convolution of 150 ms (5 pixels). For this example, we show the averaged spike rasters for each direction (Fig. 7A) and for all directions (Fig. 7B and C). The simulated data were analyzed with the algorithm, and the automatically mapped RF (Fig. 7D and E) was used to evaluate the precision of the proposed method. The RF that was mapped with the Gaussian smoothing was less noisy and more precise than the one constructed without smoothing. We found that widths that were close to the size of the expected RF produced more precise RF centers, and widths of approximately 1.8 times the expected RF were more precise in terms of RF size. Nevertheless, comparisons of the results obtained with each of these widths were not significantly different in terms of center or size.

3.3.2. Normalized measures (*z*-scores) × frequency (Hz)

The variances of neuronal responses are directly proportional to their amplitudes. As the *z*-score normalization was performed independently for each direction, more responsive directions end up being flattened compared to less responsive directions. This situation is beneficial for the study of highly orientation/direction selective neurons because it reduces the overestimations of RF size for the less responsive directions. Systematic testing showed that the *z*-score normalization significantly improved the size precision when the responses for all directions were similar, and this improvement was greater for responses with direction/orientation selective responses. We did not observe significant differences in RF center positions; although a small improvement in precision was observed when non-normalized responses were examined. Therefore, the *z*-score normalized responses generally produce more precise results overall. Additionally, as seen in a previous section, *z*-scores are useful for estimating the quality of the back-projection mapped RF.

3.4. Map accuracy: Response intensity, peak position and RF size

To test the accuracy of the back-projection mapped RFs, we simulated 10-trial sets of response data for 5 different levels of RF response intensities with peak probabilities of 0.05, 0.1, 0.15, 0.20 and 0.25 above the background (Fig. 8). For each probability, 1000 RFs were simulated. Different theoretical response level probabilities produced back-projection RFs with peak values (*z*-scores) that were positively correlated, and the variances of these back-projection RFs decreased with increasing spike probability values (Fig. 8C). The blue vertical lines indicate the *z*-scores of 1.96 and 2.58, which correspond to probabilities of 0.05 and 0.01 for large samples.

We compared two RF parameters, center position and size, obtained from the simulated data with the parameters defined by the theoretical response curves (Fig. 8A and B). As expected, there was a strong negative correlation between precision and peak responses. RF centers with errors greater than half of the RF radius composed less than 3% (0.027) of the population with *z*-scores above 1.96 and less than 0.05% of the population with *z*-scores above 2.58 (Fig. 8A). Although size errors were significant due to the size of the simulated sample, the size errors exhibited weak correlations with the response intensities and indicated that the 0.76 peak height RF size, on average, matched the half-peak height size of the theoretical RF (Fig. 8B). Nevertheless, a tendency to underestimate the RF size is seen for the lower probability data ($p = 0.05$ – ii red). Furthermore, greater absolute size errors were seen for lower peak responses (for the 0.05 spike probability, the average was 11.97%) than for higher peak responses (for the 0.25 spike probability, the average was 4.73%).

3.4.1. Number of directions and trials

The number of trials is a key factor that concerns both the quality of the averaged RF response and the stimulation time during the experiments. As the back-projection RF averages the responses for all directions, the total number of trials averaged is equal to the number of trials per direction times the number of directions used. We tested the precision of the back-projection maps constructed from the simulated data while systematically varying the number of directions and the number of trials; as expected, we found a given total number of trials produced the same precisions independent of the number of trials per direction and the number of directions. For example, RFs mapped with 8 directions and 10 trials per direction exhibited the same accuracies as RFs mapped with 16 directions and 5 trials per direction. Thus, for simplicity, we tested the influence of the number of trials on accuracy using 8 directions of stimulation. We tested trials (rasters) of RFs with spike probabilities ($p = 0.025$, 0.05 and 0.1) that were minimally above the spontaneous activity. Fig. 9 shows the variations of map peak responses (Fig. 9A) and precisions (Fig. 9B) for the three tested spike probabilities as the numbers of trials were altered. As

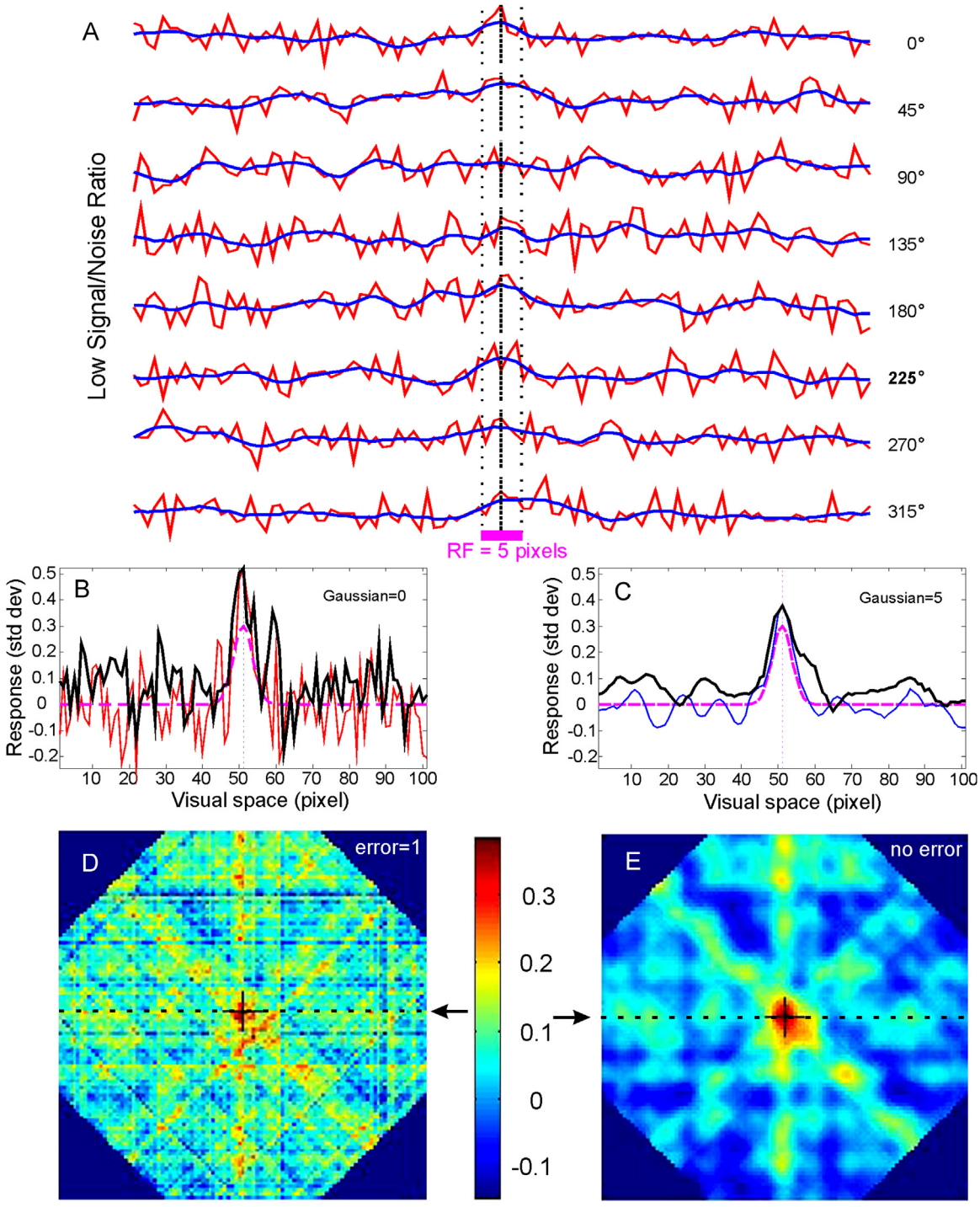

Fig. 7. Examples of automatic mapping of a 1.5° × 1.5° (5 × 5 pixels) RF from a simulated unit with low signal/noise ratio (0.3) studied with 10 trials and 8 directions. We generated an RF map without convolution (Gaussian = 0) and one with a 150 ms Gaussian (5 pixels) convolution. The averages of the PSTHs (*red line*) and the averages of the convoluted zDFs (*blue line*) of 10 trials are shown in (A); one line is shown for each direction. The location of the RF (*light purple bar*) and the location of the center (heavy dotted line) and borders (*light dotted lines*) do not allow us to find a clear correlation between the PSTH or zDF and RF location. The averages of all 8 PSTHs (red in (B) and in blue in (C)) are compared with the simulated receptive field (*purple dashed line*) and with the back-transformed response line (*solid black line*) at the level indicated by the arrows and the black dotted lines in (D) and (E). Note that even with a noise of one (1) and a signal of 0.3, the algorithm performed well and produced an error of 1 pixel (0.3°) without Gaussian convolution and no error with a 150 ms Gaussian. (For interpretation of the references to colour in this figure legend, the reader is referred to the web version of the article.)

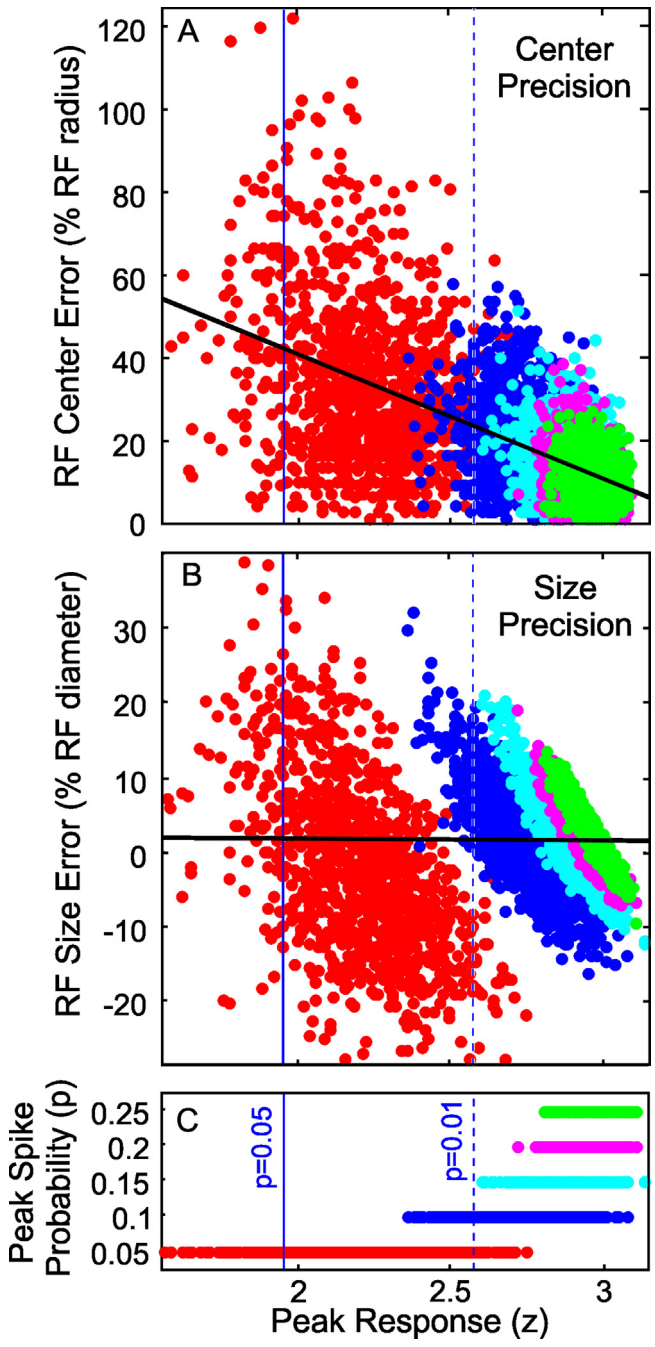

Fig. 8. Relationships between signal/noise ratios and RF center and size precisions for five groups of 1000 simulations, with different peak spike probabilities. For each peak spike probability from 5% to 25%, 1000 simulations (shown in different colors) were computed, resulting in a total of 5000 simulations. The signal/noise ratios are expressed in *z*-scores of the peak responses. The size of the RF was considered to be 73% of the peak response. RF location errors and RF center errors are expressed as the percentage of the RF radius. RF size errors are expressed as the percentage of increase (positive values) or decrease (negative values) in RF diameters.

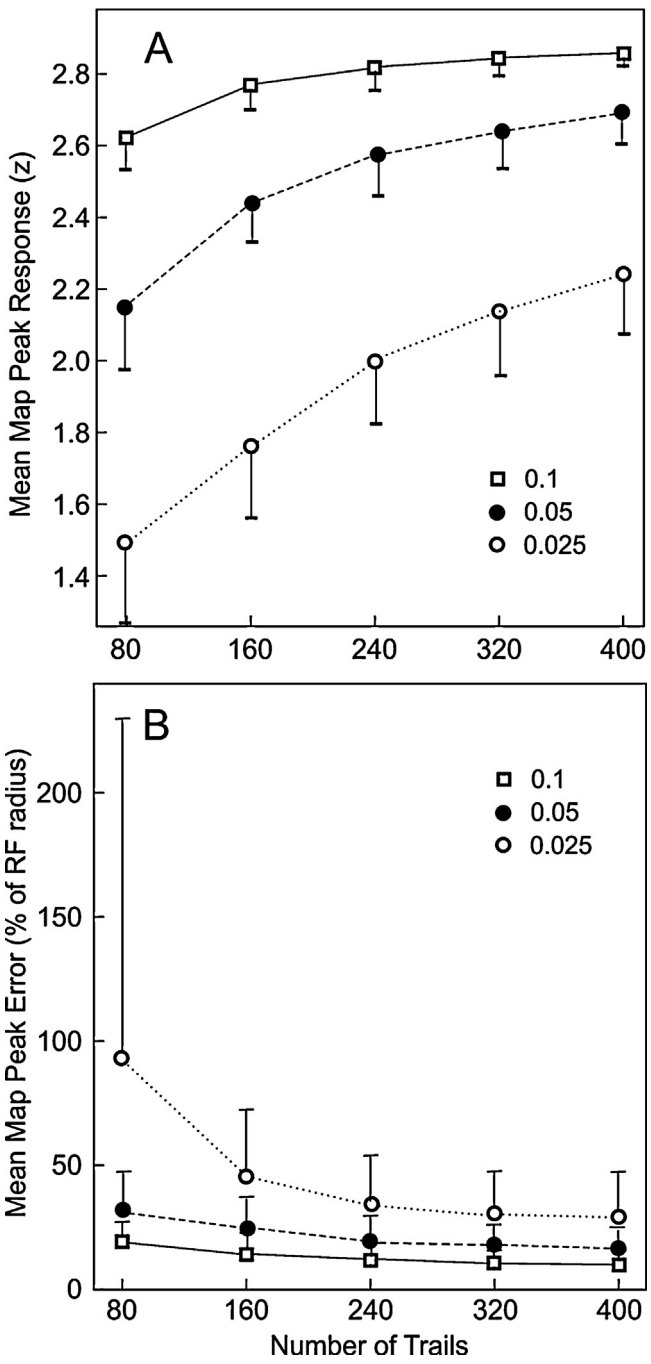

Fig. 9. Effect of the number of trials on the precisions of the mean map peak responses (A) and mean map peak errors (B) of the receptive field centers for different signal/noise ratios.

expected, less responsive RFs ($p = 0.025$) showed benefited more from increasing the number of trials. Although a minimum of 240 trials was needed to produce average *z*-scores above 1.96, the biggest improvement in map precision, especially in terms of variance, occurred at approximately 160 trials. Almost no improvement was seen above 240 trials. For higher spike probabilities (0.05 and 0.1), there was almost no improvement in map precision above 80 trials.

4. Discussion

Ringach (2004) presented a description of nine methods that have been developed over the years to map receptive fields. In this review, Ringach (2004) presented fundamental and new theoretical concepts that accompany the following methods: (1) *the linear-non-linear model and reverse correlation method* (Rodieck and Stone, 1965a,b); (2) *Gabor-like shapes and simple receptive fields* (Movshon et al., 1978; Ringach, 2002); (3) *non-linear outputs and their measurement* (Chichilnisky, 2001); (4) *spatio–temporal properties and direction selectivity* (Adelson and Bergen, 1985; Reid et al., 1987; DeAngelis et al., 1995); (5) *the gain control model* (Albrecht and Geisler, 1991; Geisler and Albrecht, 1991; Robson,

1991; Heeger, 1992); (6) *gain control and intracortical sharpening of tuning* (DeAngelis et al., 1992); (7) *the energy model and complex cells* (Spitzer and Hochstein, 1985, 1988; Adelson and Bergen, 1985); (8) *non-Gaussian models for estimating RF structures* (De Ruyter van Steveninck and Bialek, 1988; Chechik et al., 2004); and (9) *the hierarchical model and theories of cortical function* (Maffei and Fiorentini, 1973; De Valois et al., 1979; Kulikowski and Bishop, 1981; Bell and Sejnowski, 1997; Simoncelli and Olshausen, 2001; Hurri and Hyvarinen, 2003).

If one accepts the view that receptive field properties appear to lie on a continuum, it is sensible to seek theoretical models that explain the distribution of receptive field properties and their correlations across the entire population. The discreteness of neural populations in the cortex must be considered, as the final product may have a strong impact on how one views cortical organization and function.

The algorithms of the method described here can be subdivided into five steps, each with a specific purpose: (1) the PSTH (post stimulus time histogram) step based on STA (spike triggered averaging) describes the response to a moving bar; (2) *z*DF (spike density function) – Gaussian convolution of the PSTH expresses the probability of firing in response to the moving bar; (3) RDF (response density function) – division of the *z*DF by the standard deviation or by the variance of the response at each point of the trajectory of the bar expresses the responsiveness of the neuron at each point; (4) SRF (space responsive function) – averages the responsiveness in the spatial domain. (5) BTRF (back-transformed receptive field) – back-transformation of the SRF in all directions onto the visual space domain. BTRFs have previously been referred to as Quantitative Intersection Maps. This method has similarities with the linear–non-linear model and reverse correlation method (Rodieck and Stone, 1965a,b) and is related to non-linear outputs and their measurements (Chichilnisky, 2001) and the spatio–temporal properties and direction selectivity method (Adelson and Bergen, 1985; Reid et al., 1987; DeAngelis et al., 1995). Nonetheless, the BTRF method is unique, as it is different from classical STA.

4.1. Latency

We consider the neuronal response to a long stimulus passing over the neuron's RF as a linear view of the stimulated portion of the visual field taken from the point of view orthogonal to the axis of movement (similar to Fig. 2). Three points are important to consider when looking for the temporal relationship of the neuronal responses and the actual RF. First, and more obvious, is neuronal latency, which will displace the response relative to its spatial position (Fig. 3B). Second, the neurons can sustain their responses for some time after stimulation (post-responses), which will increase response profiles relative to RF sizes and add some latency to the peaks. Third, the stimulus we choose for reasons of methodological simplicity (a bar) has a measurable width, and its borders are actually two individual stimuli. In addition, the 'double' border post-response can sum in a nonlinear manner. From a methodological point of view, this third factor, the stimulus width, can be removed by using single contrast border stimuli, but these types of stimuli are more difficult to implement. The last two factors will contribute to the overall latency of the response peak, and therefore the latency value found for the RF peak and used to convert temporal coordinates into spatial coordinates will be overestimated. Moreover, even after latency correction, the last two factors will increase the size of the responsive region and result in larger mapped RFs relative to the actual RFs. A comparison of the back-projection and reverse correlation methods in primate V1 performed by Botelho et al. (2012) revealed that these methods produced similar latency and RF size values, although the resolution used in that comparison was relatively low. Furthermore, latencies in the range of 50–70 ms for the early visual areas are in accordance with other data presented in the literature (Gawne et al., 1996; Levy et al., 2013; Frégnac et al., 1994). In summary, the latencies and RF sizes obtained with the back-projection map may be used to fully represent neuronal properties, and although absolute RF latencies and sizes may be slightly overestimated, this method is still a powerful tool for comparing neurons across different conditions.

After the pioneering studies of Hubel and Wiesel (1968), new principles appeared that have changed our ideas about the importance of receptive fields (see Ringach, 2004 for review), at least those of the primary visual cortex (Volgushev et al., 1993; Mechler and Ringach, 2002; Victor et al., 2009). The back-projection method with small oriented stimuli seems adequate for the localization and mapping of the RFs of striate and extra-striate areas. However, our method uses long moving bars as stimuli. This stimulus configuration has limitations because it does not account for speed selectivity or length inhibition of RFs. Length inhibition, a reduction in responses when the stimulus is longer than the RF size, is a common feature of numerous types of visual neurons (Hubel and Wiesel, 1968). Moreover, many neurons show stimulus speed selectivity. The speed we choose, 10°/s, was the best compromise between response effectiveness and the stimulation time. Nevertheless, RF mapping will be impaired only for neurons with very strong length inhibition (i.e., those that exhibit no response to long stimuli) or neurons that are highly selective for other speeds. Receptive fields from areas that exclusively respond to moving textures, such the anterior ectosylvian visual area of the cat (Scannell et al., 1996; Benedek et al., 2000), will not be revealed by this method. Nevertheless, this method is capable of mapping RFs for nearly every recording site of the visual areas we have studied previously (V1, V2, V4 and MT).

Pipa and his colleagues (Pipa et al., 2012) studied several methods of receptive field mapping and concluded that the point-process generalized linear model (PPGLM) is a more efficient and accurate method for determining the size of the receptive field and the orientation preference of the RF than the spike-triggered averages (STA) or the first-order Wiener–Volterra Kernel (WVK) methods. These authors claim that their PPGLM model takes into account intrinsic neuronal dynamics, including absolute and relative refractory periods that are important for predicting current spiking activity (Truccolo et al., 2005, 2010). In contrast to Pipa et al. (2012), we did not use a Radon transform or the PPGLM process. Instead, we averaged the convoluted spike density functions and, using a back-transform algorithm, we integrated the response in the spatial plane. Pipa et al. (2012) argue that methods based on a classical STA and the method used here are less precise; however, we have using this method to map more than two thousand RFs in V1 with great success. We have never encountered any of the limitations mentioned by these authors. Our method has also successfully been used in primates by our group (V1 (Botelho et al., 2012); V2 and V4 (Jansen-Amorim et al., 2012); MT (Jansen-Amorim et al., 2011) and pulvinar (Soares et al., 2004)), by other groups in primate V1 (Lima et al., 2011) and in the avian visual wulst (Pinto and Baron, 2009, 2010; Baron et al., 2007).

Back-projection is an adequate method for mapping the contours of receptive fields, but it is not suitable for revealing RF structure. Our method is quite simple compared to that of Pipa et al. (2012) yet quite precise in revealing RFs for neurons with low signal-to-noise ratios. We should emphasize that Pipa et al. (2012) used experimental data that had previously been analyzed with our back-projection algorithm, and they performed a theoretical analysis that employed more sophisticated mathematics. Nonetheless, the back-projection method, as implemented here, is comprehensive, easily implemented, fast and sufficiently precise for experimental designs in which mapping the centers and borders of RFs are important.

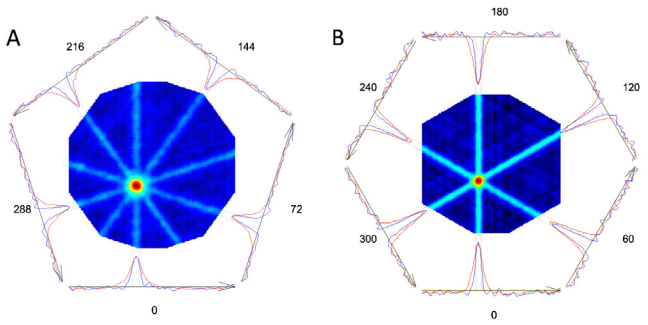

Fig. 10. Effect of the number of directions on the number of ridges and on the strength of the ridge artifacts. Odd numbers of directions increase the number of ridges but decrease the size of the ridge artifacts (A), while even numbers of directions decrease the number of ridges but increase the size of the ridge artifacts (B).

4.2. Map accuracy, number of trials and number of directions

We have seen that most RFs can be mapped with 8 directions and 10 trials per direction, resulting in a total of 80 trials being averaged in the back-projection RF (see Fig. 9). Moreover, increases in the number of trials in excess of 80 are accompanied by much slower improvements in accuracy (Fig. 9); thus, higher numbers of trials are only worthwhile in situations in which one is interested in very minimally responsive neurons (response probabilities below 0.05). Therefore, the total number of trials can be distributed in different number of directions. The increase in the number of directions diminishes the ridge artifacts because these artifacts become more diluted when averaged across a larger number of baseline activities (Fig. 10). Odd numbers of directions increase the number of ridges but decrease the ridge artifacts (compare Fig. 10A with B). However, if the total number of trials is kept constant, increases in the number of directions decrease the number of trials per direction and affect the precision of the estimated response to each direction, which may impair the estimates of the functional properties of the neurons because it is important to record at least 10 trials per direction to attain reasonable precision. In summary, 8 directions with 10 trials per direction seem appropriate for mapping RFs and coarsely inferring functional properties. If finer functional inferences are required, the number of directions should be increased, and a minimum of 10 trials per direction should be maintained.

4.3. Map artifacts and RF size and shape

The back-projection maps show ridge artifacts and enlarged response profiles. Computer tomography uses continuous data acquisition from different directions ('infinite directions') to remove ridge artifacts; however, the back-projection technique enlarges these contours. Filtered back-projection can be used to remove this enlargement. Filtering the data with an appropriate difference of Gaussians (DOG) wavelet can restore the sizes in the map. The DOG approximates the 'Mexican Hat wavelet' by subtracting a wide Gaussian from a narrow Gaussian. This filtering can be performed in different steps of constructing the back-projection map data both pre- and post-processing. Filtered back-projection may help to define the correct RF size when the responses are robust but impairs center and size map precision at low levels of responsiveness (this is particularly true for the center precision). Therefore, non-filtered back-projection is more robust and may be used to find RFs independent of the activity level.

For orientation/direction selective neurons, the back-projection map RFs may have an elliptical shape even when using z-scores calculated independently for each direction. Although most direction/orientation selective RFs are actually elliptical (Hubel and Wiesel, 1968), the back-projection map may make exaggerate the ellipse; i.e., the map may underestimates size in the directions with good responses and overestimate size in the directions with weaker responses. As RF size along the map response profile defines the interval over which the average response for each direction in the histograms is computed, underestimations in size imply the averaging of more responses that are close to the peak, which will lead to overestimations of the average response for the more responsive directions. The opposite will occur for RF size overestimation and lead to underestimation of average responses. This effect acts to potentiate the indices, such as a scaling factor; i.e., more selective responses will have disproportionally larger measurements. As we have indicated previously, RF size can be corrected by appropriate filtering or by varying the height of the cut level for different directions; however, these techniques only work well for large responses. Although the back-projected RF shape is somewhat inaccurate for inferring the real selectivity, it produces consistent values for similar response configurations and can be used to compare functionally different neuronal populations. Additionally, this scaling factor better differentiates functional selectivity (increases variance), which should help to differentiate neuronal populations.

5. Conclusion

This study revealed the following properties of the back-projection method: it is comprehensive and easy to implement; it is precise in locating RF positions; it provides consistent information about RF shapes and sizes, which will allow for comparative studies; it is sensitive and can map RFs with quite low responses; it can scan for RFs in an extensive area of the visual field; it is very fast; it provides functional properties; and it can map RFs in regions without direct retinal inputs, such as the cortical representations of the optic disc and retinal lesions. Therefore, the back-projection mapping method is a good choice for quantitative topographic studies, especially those involving wide areas of the visual field or regions lacking direct retinal input. Although this method is not suited for RF structure studies, it should still be a first-choice method for locating the region of interest before initiating more refined mapping procedures. Additionally, this method's ease of implementation and speed make it a good alternative to the manual qualitative mapping methods that are still widely used, and the use of this method will increase the precision and reproducibility of experimental results.

Appendix A. Algorithm to obtain the quantitative response intersection map

```
function map = back_project(data, directions, method)
% BACK_PROJECT Returns a back-projected MAP of the
%                          intersected DATA.
% MAP = back_project(DATA, DIRECTIONS, <METHOD>);
% MAP is a square array (DATA length x DATA length)
%        of the intersected (averaged) DATA.
%        obs. it uses array coordinates (ij). To see (plot) it
%              use: [axis ij] or plot a flipped MAP [flipud(MAP)].
% DATA is an array of N lines, representing the vectors
%        (projections) to be intersected.
% DIRECTIONS are the N stimulus directions for the N DAT vectors,
%                          in DEGREES (zero at left, counterclockwise).
% METHOD <optional>: 0 = ARITHMETIC (default);
%                                    1 = GEOMETRIC(*);
%                                    2 = PRODUCT.
% (*)negative number sigs are removed before rooting and then reassigned.
%
% mario fiorani, last modified November 2012 (first version, 2001)

if (size(data,1) ~= numel(directions)), error('dimension mismatch'), end
if (nargin == 2), method = 0; end
sz = size(data,2);
```

```
pad = ceil((sqrt(2)*sz-sz)/2);
pad_dat(1:sz + 2*pad) = nan;
cj = repmat(-(sz-1)/2:1:(sz-1)/2, sz, 1);
ci = cj';
map(1:sz,1:sz) = ~~method;
for n = 1:length(directions),
  t = directions(n)*pi/180;
  pad_dat(pad + 1:pad + sz) = data(n,:);
  rcj = round(cj*cos(t) - ci*sin(t) + ceil(pad + sz/2));
  dat_array = pad_dat(rcj);
  if method, map = map.*dat_array; else map = map + dat_array; end
end
switch method,
case 0, map = map./n;
case 1, s = sign(map); in = isnan(map); map(in) = 1;
  map = abs(map).^(1/n).*s; map(in) = nan;
end
```

References

Adelson EH, Bergen JR. Spatiotemporal energy models for the perception of motion. J Opt Soc Am A 1985;2:284–99.

Albrecht DG, Geisler WS. Motion selectivity and the contrast-response function of simple cells in the visual cortex. Vis Neurosci 1991;7:825–37.

Barlow HB, Blakemore C, Pettigrew JD. The neural mechanism of binocular depth discrimination. J Physiol 1967;193:327–42.

Baron J, Pinto L, Dias MO, Lima B, Neuenschwander S. Directional responses of visual wulst neurones to grating and plaid patterns in the awake owl. Eur J Neurosci 2007;26:1950–68.

Bell AJ, Sejnowski TJ. The 'independent components' of natural scenes are edge filters. Vision Res 1997;37:3327–38.

Benedek G, Sztriha L, Kovács G. Coding of spatial co-ordinates on neurones of the feline visual association cortex. NeuroReport 2000;11:1381–4.

Botelho EP, Ceriatte C, Soares JGM, Gattass R, Fiorani M. Quantification of early stages of cortical reorganization of the topographic map of V1 following retinal lesions in monkeys. Cereb Cortex 2012., http://dx.doi.org/10.1093/cercor/bhs208.

Chechik G, Globerson A, Tishby N, Weiss Y. Information bottleneck for Gaussian variables. In: Thrun S, Lawrence S, Schölhopf B, editors. Advances in Neural Information Processing Systems 16. Cambridge, MA: MIT Press; 2004.

Chichilnisky EJ. A simple white noise analysis of neuronal light responses. Network 2001;12:199–213.

Colby CL, Duhamel JR, Goldberg ME. Visual, presaccadic, and cognitive activation of single neurons in monkey lateral intraparietal area. J Neurophysiol 1996;76:2841–52.

Das A, Gilbert CD. Receptive field expansion in adult visual cortex is linked to dynamic changes in strength of cortical connections. J Neurophysiol 1995;74:779–92.

De Ruyter van Steveninck R, Bialek W. Real-time performance of a movement-sensitive neuron in the blowfly visual systemm: coding and information transfer in short spike sequences. Proc R Soc Lond B Biol Sci 1988;234:379–414.

De Valois KK, De Valois RL, Yund EW. Responses of striate cortex cells to grating and checkerboard patterns. J Physiol 1979;291:483–505.

DeAngelis GC, Ohzawa I, Freeman RD. Receptive-field dynamics in the central visual pathways. Trends Neurosci 1995;18:451–8.

DeAngelis GC, Robson JG, Ohzawa I, Freeman RD. Organization of suppression in receptive fields of neurons in cat visual cortex. J Neurophysiol 1992;68:144–63.

Dow BM, Snyder AZ, Vautin RG, Bauer R. Magnification factor and receptive field size in foveal striate cortex of the monkey. Exp Brain Res 1981;44:213–28.

Duhamel JR, Colby CL, Goldberg ME. Ventral intraparietal area of the macaque: congruent visual and somatic response properties. J Neurophysiol 1998;79:126–36.

Duhamel JR, Bremmer F, Ben Hamed S, Graf W. Spatial invariance of visual receptive fields in parietal cortex neurons. Nature 1997;389:845–8.

Fiorani M, Gattass R, Rosa MGP, Souza APB. Visual area MT in the Cebus monkey: location, visuotopic organization and individual variability. J Comp Neurol 1989;287:98–118.

Frégnac Y, Burke JP, Smith D, Friedlander MJ. Temporal covariance of pre- and postsynaptic activity regulates functional connectivity in the visual cortex. J Neurophysiol 1994;71:1403–21.

Gattass R, Gross CG. Visual topography of striate projection zone (MT) in posterior superior temporal sulcus of the macaque. J Neurophysiol 1981;46:621–38.

Gawne TJ, Kjaer TW, Richmond BJ. Latency: another potential code for feature binding in striate cortex. J Neurophysiol 1996;76:1356–60.

Geisler WS, Albrecht DG. Cortical neurons: isolation of contrast gain control. Vision Res 1991;32:1409–10.

Gilbert CD, Das A, Ito M, Kapadia M, Westheimer G. Spatial integration and cortical dynamics. Proc Natl Acad Sci U S A 1996;93:615–22.

Heeger DJ. Normalization of cell responses in cat striate cortex. Vis Neurosci 1992;9:181–97.

Herman GT. Fundamentals of Computerized Tomography: Image Reconstruction from Projection. second ed. Berlin: Springer; 2009.

Hubel DH, Wiesel TN. Receptive fields and functional architecture of monkey striate cortex. J Physiol 1968;195:215–43.

Hubel DH, Wiesel TN. Receptive fields, binocular interaction and functional architecture in the cat's visual cortex. J Physiol 1962;160:106–54.

Hubel DH, Wiesel TN. Uniformity of monkey striate cortex: a parallel relationship between field size, scatter, and magnification factor. J Comp Neurol 1974;158:295–305.

Hurri J, Hyvarinen A. Simple-cell-like receptive fields maximize temporal coherence in natural video. Neural Comput 2003;15:663–91.

Jansen-Amorim AK, Fiorani M, Gattass R. GABA inactivation of area V4 changes receptive-field properties of V2 neurons in Cebus monkeys. Exp Neurol 2012;235:553–62.

Jansen-Amorim AK, Lima B, Fiorani M, Gattass R. GABA inactivation of visual area MT modifies the responsiveness and direction selectivity of V2 neurons in Cebus monkeys. Vis Neurosci 2011;28:513–27.

Kulikowski JJ, Bishop PO. Fourier analysis and spatial representation in the visual cortex. Experientia 1981;37:160–3.

Levy M, Fournier J, Frégnac Y. The role of delayed suppression in slow and fast contrast adaptation in V1 simple cells. J Neurosci 2013;33:6388–400.

Lima B, Singer W, Neuenschwander S. Gamma responses correlate with temporal expectation in monkey primary visual cortex. J Neurosci 2011;31:15919–31.

Maffei L, Fiorentini A. The visual cortex as a spatial frequency analyser. Vision Res 1973;13:1255–67.

Mechler F, Ringach DL. On the classification of simple and complex cells. Vision Res 2002;42:1017–33.

Movshon JA, Thompson ID, Tolhurst DJ. Spatial summation in the receptive fields of simple cells in the cat's striate cortex. J Physiol 1978;283:53–77.

Palmer LA, Jones JP, Gottschalk AG. Constraints on the Estimation of Receptive-field Profiles of Simple Cells in Visual Cortex. Advanced Methods of Physiological System Modeling. Cambridge: Cambridge University Press; 1987. p. 115–35.

Pinto L, Baron J. Spatiotemporal frequency and speed tuning in the owl visual wulst. Eur J Neurosci 2009;30:1251–68.

Pinto L, Baron J. Spatiotemporal frequency tuning dynamics of neurons in the owl visual wulst. J Neurophysiol 2010;103:3424–36.

Pipa G, Chen Z, Neuenschwander S, Lima B, Brown EN. Mapping of visual receptive fields by tomographic reconstruction. Neural Comput 2012., http://dx.doi.org/10.1162/NECO_a_00334.

Reid RC, Soodak RE, Shapley RM. Linear mechanisms of directional selectivity in simple cells of cat striate cortex. Proc Natl Acad Sci U S A 1987;84:8740–4.

Ringach DL. Mapping receptive fields in primary visual cortex. J Physiol 2004;558:717–28.

Ringach DL. Spatial structure and symmetry of simple-cell receptive fields in macaque primary visual cortex. J Neurophysiol 2002;88:455–63.

Robson JG. Neural coding of contrast in the visual system. Opt Soc Am Techn Digest System 1991;17:152.

Rodieck RW, Stone J. Analysis of receptive fields of cat retinal ganglion cells. J Neurophysiol 1965a;28:832–49.

Rodieck RW, Stone J. Response of cat retinal ganglion cells to moving visual patterns. J Neurophysiol 1965b;28:819–32.

Scannell JW, Sengpiel F, Tovée MJ, Benson PJ, Blakemore C, Young MP. Visual motion processing in the anterior ectosylvian sulcus of the cat. J Neurophysiol 1996;76:895–907.

Simoncelli EP, Olshausen BA. Natural image statistics and neural representation. Annu Rev Neurosci 2001;24:1193–216.

Smith SW. The Scientist and Engineer's Guide to Digital Signal Processing. second ed. San Diego: California Technical Publishing; 1999. p. 442–50.

Soares JGM, Diogo AC, Fiorani M, Souza AP, Gattass R. Effects of inactivation of the lateral pulvinar on response properties of second visual area cells in Cebus monkeys. Clin Exp Pharmacol Physiol 2004;31:580–90.

Spitzer H, Hochstein S. A complex-cell receptive-field model. J Neurophysiol 1985;53:1266–86.

Spitzer H, Hochstein S. Complex-cell receptive field models. Prog Neurobiol 1988;31:285–309.

Talbot SA, Marshall WH. Physiological studies on neural mechanisms of visual localization and discrimination. Am J Ophthal 1941;24:1255–63.

Truccolo W, Hochberg LR, Donoghue JP. Collective dynamics in human and monkey sensorimotor cortex: predicting single neuron spikes. Nat Neurosci 2010;13:105–11.

Truccolo W, Eden UT, Fellow M, Donoghue JP, Brown EN. A point process framework for relating neural spiking activity to spiking history, neural ensemble and covariate effects. J Neurophysiol 2005;93:1074–89.

Victor JD, Mechler F, Ohiorhenuan I, Schmid AM, Purpura KP. Laminar and orientation-dependent characteristics of spatial nonlinearities: implications for the computational architecture of visual cortex. J Neurophysiol 2009;102:3414–32.

Volgushev M, Pei X, Vidyasagar TR, Creutzfeldt OD. Excitation and inhibition in orientation selectivity of cat visual cortex neurons revealed by whole-cell recordings in vivo. Vis Neurosci 1993;10:1151–5.